Composites Science and Technology 261 (2025) 110991

Contents lists available at ScienceDirect

Composites Science and Technology

journal homepage: www.elsevier.com/locate/compscitech

Tailoring the interfacial properties of glass fiber-epoxy microcomposites through the development of a self-healing poly(ϵ-caprolactone) coating

Laura Simonini [a,b,*], Markus Kakkonen [c], Royson Dsouza [d], Mikko Kanerva [e], Haroon Mahmood [a,b], Andrea Dorigato [a,b], Alessandro Pegoretti [a,b]

[a] Department of Industrial Engineering, University of Trento, via Sommarive 9, 38123, Trento, Italy
[b] National Interuniversity Consortium of Materials Science and Technology (INSTM), Via Giusti 9, 50121, Florence, Italy
[c] Fibrobotics Oy, Korkeakoulunkatu 1, 33720, Tampere, Finland
[d] VTT Technical Research Centre of Finland Ltd, Vuorimiehentie 2, 02150, Espoo, Finland
[e] Faculty of Engineering and Natural Sciences, Tampere University, Korkeakoulunkatu 6, 33720, Tampere, Finland

ARTICLE INFO

Keywords:
Self-healing
Microdebonding
Polycaprolactone
Glass fibers
Interfacial adhesion

ABSTRACT

The aim of this study was the development and characterization of a continuous poly(ϵ-caprolactone) (PCL) coating, which was applied on glass fibers by a fluid coating method, in order to tailor the interfacial properties in glass fiber-epoxy microcomposites. Scanning electron microscopy revealed that a uniform coating was formed without noticeable discontinuities or irregularities, and its thickness increased with the deposition speed. To achieve consistent results with this approach, it is essential to consider the homogeneity of the coating thickness, which is influenced by the viscosity of the solution. The PCL-coated fibers were used for the preparation of microcomposites combined with epoxy resin (EP). The samples were tested in the microdebonding configuration to determine the interfacial shear strength (IFSS) and to assess their interfacial self-healing capability. For all deposition speeds, no significant degradation of interfacial adhesion was observed indicating the applicability of PCL coating on glass fibers. However, a decrease in self-healing efficiency was observed after multiple self-healing stages. The possible cause was identified in the progressive alteration of the EP droplet's shape after repeated microdebonding tests. This phenomenon altered the stress distribution along the fiber-matrix contact area and, therefore, underestimated the values of interfacial adhesion and self-healing efficiency. Hence, the experimental results from microdebonding tests were presented along with a finite element analysis of the interfacial region, in order to provide a comprehensive understanding of the debonding and self-healing mechanisms after multiple repairing steps.

1. Introduction

The request for improved mechanical, thermal, electrical and chemical properties of materials is driving the research towards the creation of advanced polymer matrix composites (PMCs) [1–3], whose market is particularly developed in the transportation [4], construction [5] and renewable energy sectors [6]. PMCs consist of a matrix, either thermosetting or thermoplastic, and a reinforcing phase, typically with fibrous morphology [7]. The region where they physically and chemically interact is called interphase [8]. Usually, fibers such as glass, carbon, and basalt have significantly higher mechanical properties than the matrix [9]. Consequently, when stress is applied to the composite, efficient stress transfer from the matrix to the fibers is typically desired, but this can only occur in the presence of strong interfacial adhesion [8]. The latter is established by different types of interactions, such as molecular interdiffusion or entanglement, chemical bonding, electrostatic attraction and mechanical interlocking [10]. When these interactions are weak, debonding can occur and it can potentially lead to a premature failure of the composite. Therefore, the improvement of the interfacial adhesion and the simultaneous incorporation of interfacial self-healing properties are of utmost importance.

Microbond tests are experimental methods at the microscale used to investigate the fiber-matrix interfacial adhesion. These tests include single-fiber fragmentation, single-fiber push-out, single fiber pull-out and microdebonding [1]. In particular, microdebonding (MB) test applies load via blades in contact with matrix microdroplets deposited on

* Corresponding author. Department of Industrial Engineering, University of Trento, via Sommarive 9, 38123, Trento, Italy.
E-mail address: laura.simonini@unitn.it (L. Simonini).

https://doi.org/10.1016/j.compscitech.2024.110991
Received 19 July 2024; Received in revised form 18 October 2024; Accepted 1 December 2024
Available online 2 December 2024

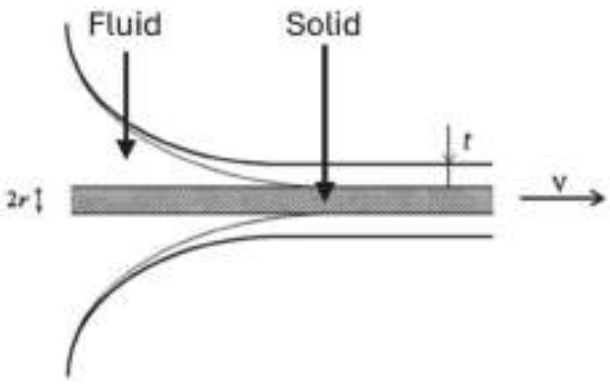

Fig. 1. Schematic image of the deposition of a PCL film on GF. Adapted from Quere [42].

single fibers, in order to induce interfacial debonding and to measure the interfacial shear strength (IFSS) at full debond [11,12]. Improvements of IFSS can be achieved through the modification of the interphase by operating either in the bulk matrix or on the fiber surface [1,13,14]. In the first case, the enrichment of the matrix with nanofillers, such as silica particles or graphene-derived nanoplates and tubes, provides specific functional groups at the interphase that can interact with those on the fiber surface. For example, Hossain et al. [15] improved the interlaminar adhesion of carbon fiber reinforced epoxy composites by 22 wt% by adding amino functionalized carbon nanotubes in the matrix. Alternatively, the formation of nanoscale phase-separated thermosetting and thermoplastic regions in the matrix creates different functionalized patterns along the fiber length to mitigate local stresses at the interphase. Czigany et al. [16] strongly improved the interfacial adhesion between basalt fiber and a vinylester-epoxy matrix through the creation of an interpenetrating network (IPN) along the fibers-matrix interface. On the other hand, the physical or chemical modification of fiber surface can enhance the mechanical and chemical interlocking on the fiber by the matrix. Various options are proposed, including surface chemical modification [17], laser treatment [18], nanocoating deposition [12] and polymeric coating deposition [11,19]. In particular, the polymeric coating deposition offers various possibilities to modify the surface of the reinforcing fibers using monomers, oligomers, and polymers [1]. This strategy aims to enhance the cohesive interactions between the polymer-coated fiber and the matrix while tuning the interphase properties as needed. In fact, it allows to create an interphase with gradient structure, which gradually changes its properties from the fiber surface toward the bulk matrix. Consequently, this approach enables the design of a multifunctional interphase, which not only fulfils the traditional role of enhancing the interfacial adhesion, but can also assume additional functions such as self-healing [20].

In the context of this study, particular emphasis is placed on the self-healing function. Self-healing systems are a class of innovative materials that have the inherent ability to fully or partially recover their original mechanical properties after being damaged [21,22]. Initially, self-healing mechanisms were primarily explored for the modification of the polymeric matrix before focusing on the interphase [23–25]. However, as mentioned earlier, the interphase is often the weakest region in composites where failure initiates, and therefore it is essential to provide self-healing capabilities in the contact region between fiber and matrix. In particular, self-healing materials are classified into two main categories: (i) extrinsic and (ii) intrinsic self-healing systems [1]. In extrinsic self-healing systems, the healing agent is contained in discrete capsules [26–28] that are deposited on the fiber surface as a discontinuous coating. For example, Jones et al. [29] studied the recovery of the fiber-matrix interfacial strength by using microcapsules of epoxy resin and ethyl-phenylacetate (EPA) solvent applied as a coating on glass fibers. On the other hand, intrinsic self-healing systems possess the capability to self-heal when triggered by the damage itself or by an external stimulus, such as heat [30–33]. The mechanisms involved in intrinsic self-healing include molecular diffusion with entanglements, reversible polymerization, melting of a thermoplastic phase, hydrogen or ionic bonding. Since these mechanisms are reversible, multiple healing events are possible [34], unlike the extrinsic self-healing systems. Thermoplastic polymers are excellent candidates for intrinsic self-healing systems at composite interphase. In particular, polycaprolactone (PCL) is attractive due to the following reasons: (i) it demonstrates strong physical and chemical compatibility with glass and epoxy resin [35–37], which ensures its integration in composite structures; (ii) it possesses a remarkably low melting temperature, typically around 60 °C [38], which allows the material to melt and easily flow into the crack to be repaired; (iii) it is highly soluble different solvents [39], which makes its processability very easy [40].

Therefore, for the first time, the aim of this work was to tailor the interfacial properties of PMCs through the development of a functional thermoplastic PCL interphase as a continuous coating for glass fibers. In this context, PCL was deposited on glass fibers by following the fluid coating technique and it was characterized from a microstructural point of view. The fiber-matrix adhesion and the self-healing efficiency were determined by microdebonding tests performing up to three consecutive debonding-healing stages. The experimental results were presented along with a finite element (FE) analysis of the interfacial region, to provide a comprehensive understanding of the interfacial debonding and self-healing mechanisms after repeated events.

2. Experimental part

2.1. Materials

WINDSTRAND® glass fibers (GFs), with bundle tex equal to 600 and fiber diameter equal to 19.6 ± 0.3 μm, were provided by Owens Corning Inc. (Chambéry, France) as unsized fibers. The following properties of the fibers were experimentally evaluated: density of 2.3 ± 0.1 g/cm^3, elastic tensile modulus of 69 ± 5 GPa, tensile strength of 1944 ± 116 MPa.

An epoxy base (EC 157.1) and an aminic hardener (W 342) were provided by Elantas Italia S.r.l. (Collecchio, Italy) and they were used as the matrix. From technical datasheet, they had viscosity of 600 mPas and 30 mPas, respectively, and density of 1.14 g/cm^3 and 0.94 g/cm^3, respectively. The two components were mixed at a weight ratio of 100:30 and then cured for 40 h at 50 °C. This specific curing process was determined to be the optimal for this system after conducting preliminary experiments [40]. The following properties of cured epoxy were determined experimentally: glass transition temperature (T_g) of 80 °C, thermal degradation temperature of 352 °C, elastic modulus of 3.1 ± 0.2 GPa, tensile strength of 61 ± 15 MPa.

Poly(ϵ-caprolactone) (PCL) was provided by Polysciences Inc. (Warrington, PA, USA) in the form of 3 mm pellets and it was used as the interfacial self-healing agent. From technical datasheet, PCL had density of 1.1 g/cm^3 and number average molecular weight (M_w) of 80000 g/mol. It had a glass transition temperature (T_g) of −68 °C and a melting temperature (T_m) of 60 °C.

Dimethylformamide (DMF), having density of 0.94 g/cm^3 and purity of 99.8 %, and tetrahydrofuran (THF) having density of 0.89 g/cm^3 and purity of ≥99.9 % were purchased by Sigma Aldrich Co. (Missouri, USA) and were used as solvents for PCL.

All the materials were used as received.

2.2. Sample preparation

PCL was dissolved in a mixture of DMF:THF equal to 30:70 by weight, to obtain a 10 %wt PCL liquid solution [40]. The solution was stirred at room temperature for 4 h at 300 rpm until complete dissolution. Subsequently, the solution was degassed for 10 min to eliminate

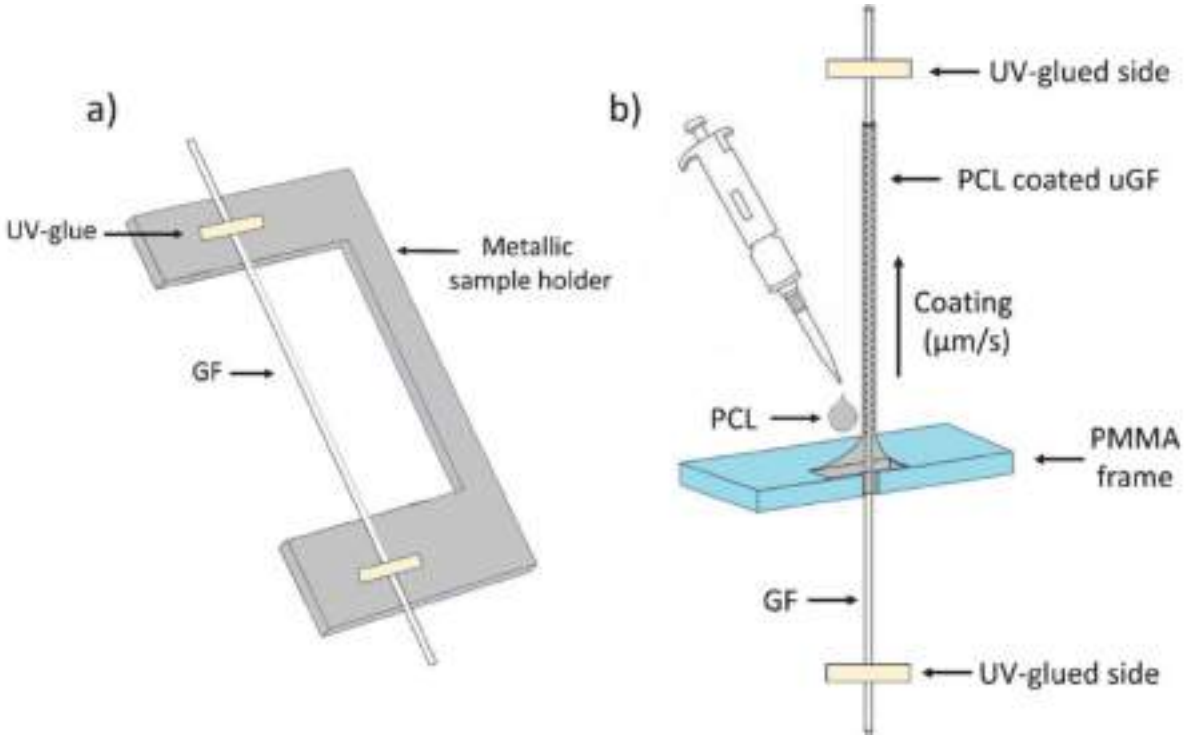

Fig. 2. (a) GF attached to a metallic sample holder, (b) schematization of the coating process where GF is forced to pass through the PCL liquid solution at a defined coating speed.

Table 1
List of the prepared coated glass fibers.

Sample	Coating speed (μm/s)
0_GF[a]	0
500_GF	500
1000_GF	1000
2000_GF	2000
2500_GF	2500
3000_GF	3000
3500_GF	3500

[a] Uncoated GF.

the air bubbles formed during the stirring process.

The fibers were coated following the fluid coating theory, where a fluid is forced to coat a solid while the latter is in movement (Fig. 1). According to this theory, the thickness of the coating (t) depends on the speed of the solid (v), referred in this work as "coating speed", when the viscosity of the fluid is constant. In fact, higher coating speeds result in thicker coatings [41]. This phenomenon has been explained in detail by Quere [42].

Particularly in this work the fluid was represented by the PCL liquid solution, while the solid was represented by a single GF. The GF was attached to a custom metallic sample holder using UV light-cured glue (Fig. 2a) and forced to pass through a droplet of the PCL liquid solution that was manually deposited on a fixed perforated poly(methyl methacrylate) (PMMA) frame (Fig. 2b). This setup was part of a Fibrodrop® apparatus (Fibrobond Oy, Tampere, Finland). The coating speed was set at 0, 500, 1000, 2000, 2500, 3000, 3500 μm/s.

The PCL-coated GFs were dried overnight at room temperature and at atmospheric pressure. The obtained samples are listed in Table 1.

Since samples were subjected to repeated self-healing stages (see Section 2.3.5), each repair stage was identified by a label (H0, H1, H2 and H3) added next to the name of the sample.

2.3. Experimental techniques

2.3.1. Brookfield viscosity measurements

The rheological properties of the PCL liquid solution were analysed through the Anton Paar MCR 301 (Anton Paar Inc., Graz, Austria) rheometer, equipped with coaxial cylinders of diameter 17 mm. Tests were carried out at 24 °C at a constant angular frequency of 100 rad/s.

2.3.2. Field-emission scanning electron microscopy (FESEM)

The morphological analysis of the fibers was carried out by a Jeol JSM-IT500 field-emission scanning electron microscope (Jeol Inc., Tokio, Japan), which operates at an acceleration voltage of 10 kV. Prior to the analysis, the samples were coated with a Pt–Pd alloy (80:20) with a thickness of about 4 nm to make them electrically conductive.

2.3.3. Atomic force microscopy (AFM)

The surface topography of the prepared samples was studied using the NT-MDT Solver Pro AFM microscope (NT-MDT Inc., Tempe, USA) equipped with a Nova scanner (Novascan Thecnologies Inc., Boone, North Carolina, USA). Images were collected in intermittent-contact mode using silicon tips (NSG-10, NT-MDT, 10 nm nominal tip radius, resonance frequency of 181 kHz). 20 × 20 μm^2 (512 × 512 pixels) topography scans were collected paying attention to land on the top of the GFs, in order to avoid areas outside the 4 μm scanner's Z range. Data representation and statistical analysis were performed with the support of Gwyddion analysis software (Metrology Institute, Brno, Czech Republic). The arithmetical mean roughness (R_a) and the root-square-mean roughness (R_q) were measured in the axial and the orthogonal direction of the fibers by following ISO 4287 standard.

2.3.4. Optical Projection Tomography (OPT)

Optical projection tomography (OPT) was employed to have a three-dimensional (3D) reconstruction of microcomposites in order to evaluate the 3D morphology of the prepared samples needed for an efficient microdebonding tests. Brightfield OPT was performed with a Fibroopt®

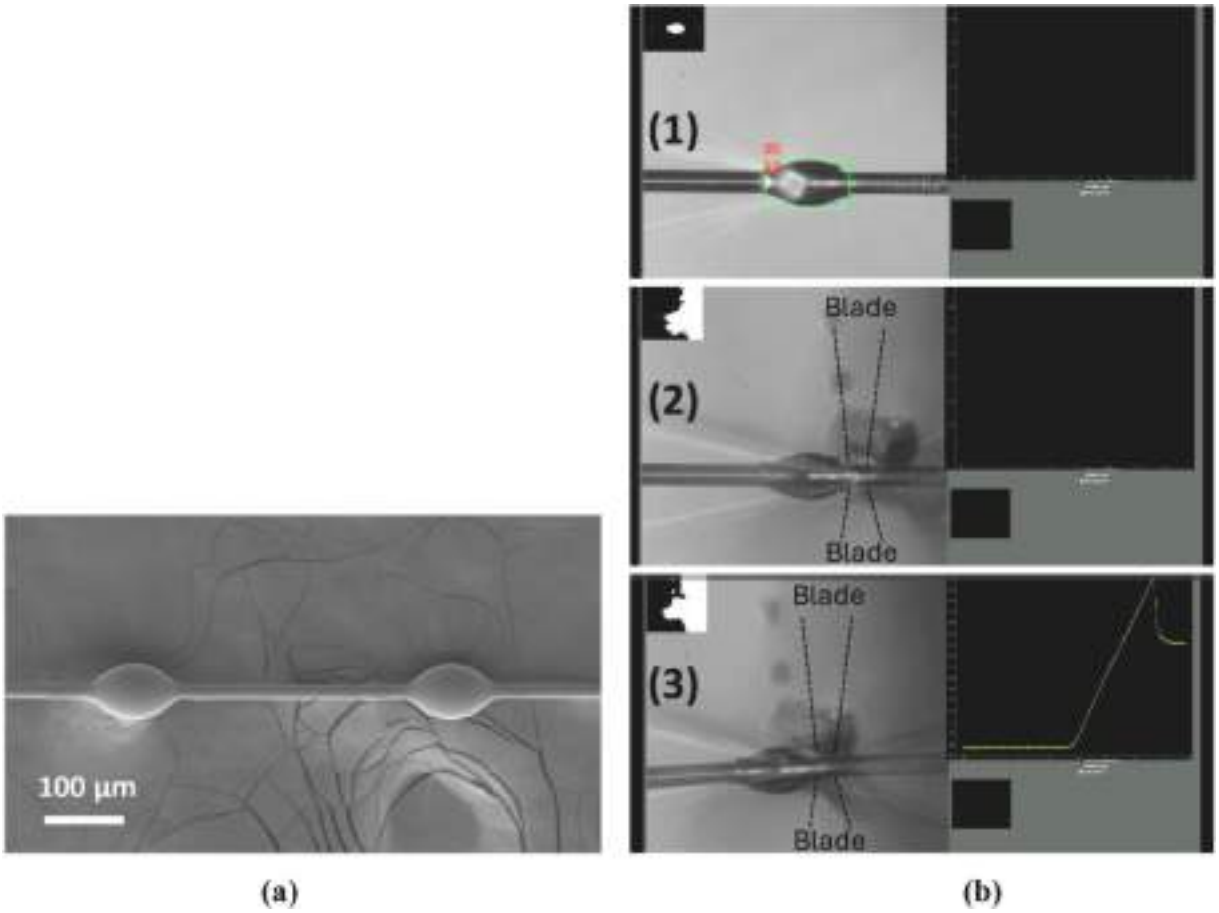

Fig. 3. Representation of (a) a microdebonding sample with two consecutive microdroplets, (b) and of microdebonding test: (1) auto-evaluation of the embedded length, (2) manual adjustment of the blades at droplet's tip, (3) microdebonding test up to debonding and data recording.

Table 2
List of constituents and parameters used in FE assembly.

Constituent	Young's Modulus (E) (GPa)	Poisson's ratio (υ)	Element type (Code)	Material type
FBG	70	0.22	8-node linear brick (C3D8R)	Linear elastic
GF	69	0.22	8-node linear brick (C3D8)	Linear elastic
EP	3.05	0.31	8-node linear brick (C3D8)	Elastic-isotropic plastic
EP-10PCL	1.54	0.39	8-node linear brick (C3D8)	Elastic – isotropic plastic
PCL	0.33	0.44	8-node linear brick (C3D8)	Elastic – perfectly plastic
Blades	220	0.29	8-node linear brick (C3D8R)	Rigid body
Sample holder	3.2	0.37	8-node linear brick (C3D8R)	Linear elastic
UV light-cured glue	1.6	0.29	8-node linear brick (C3D8R)	Linear elastic

apparatus (Fibrobotics Oy, Tampere, Finland) equipped with a tube microscope with 2x extender tube manufactured by Navitar Inc. (New York, USA) and with a 20x long working distance objective manufactured by Mitotuyo Co. (Sakado, Japan). The setup's optical scale was 0.244 µm/px (500 µm × 500 µm field of view). The systems consisted of two rotary manipulators that rotated the sample accurately around its longitudinal axis to capture the view from the angle perpendicular to the rotational axis. A total of 420 images were recorded from full rotation, with an angle difference (step) of 0.857° between images. A stack of images was processed with Fibroopt® software which utilized open source Tomopy library (Python) for reconstruction.

2.3.5. Microdebonding (MB) tests

The interfacial shear strength (IFSS) of microdebonding samples was assessed by a Fibrobond® apparatus (Fibrobotics Oy, Tampere, Finland), equipped with a load cell of 1 N. Epoxy droplets, ranging in diameter from 30 µm to 150 µm were manually applied and cured on individual GF at 50 °C for 40 h, as shown in Fig. 3a. The droplets were adequately spaced along the fiber to facilitate multiple microdebonding tests, leaving approximately 350 µm between subsequent droplets. After curing, the embedded length of the droplets was automatically measured by the optical setup incorporated in the Fibrobond® apparatus (Fig. 3b–1), which consisted of a microscope with a 20x long working distance objective and a 2x extender tube manufactured by Qioptiq GmbH (Feldkirchen, Germany). The view was recorded with an UI-3770SE monochromatic camera manufactured by IDS GmbH (Obersulm, Germany). The optical setup scale factor was 0.137 µm/px (280.576 µm × 280.576 µm field of view). Then the droplets were debonded by blades positioned at the droplet tip as shown in Fig. 3b–2. Microdebonding was performed at a displacement rate of 8 µm/min (Fig. 3b–). A comprehensive description of the device and of the methodology employed is provided by Laurikainen et al. [43]. Approximately 15–25 droplets were debonded on each fiber, with a total of ten fibers tested per sample, resulting in a cumulative dataset of approximately 150–250 debonded droplets for sample.

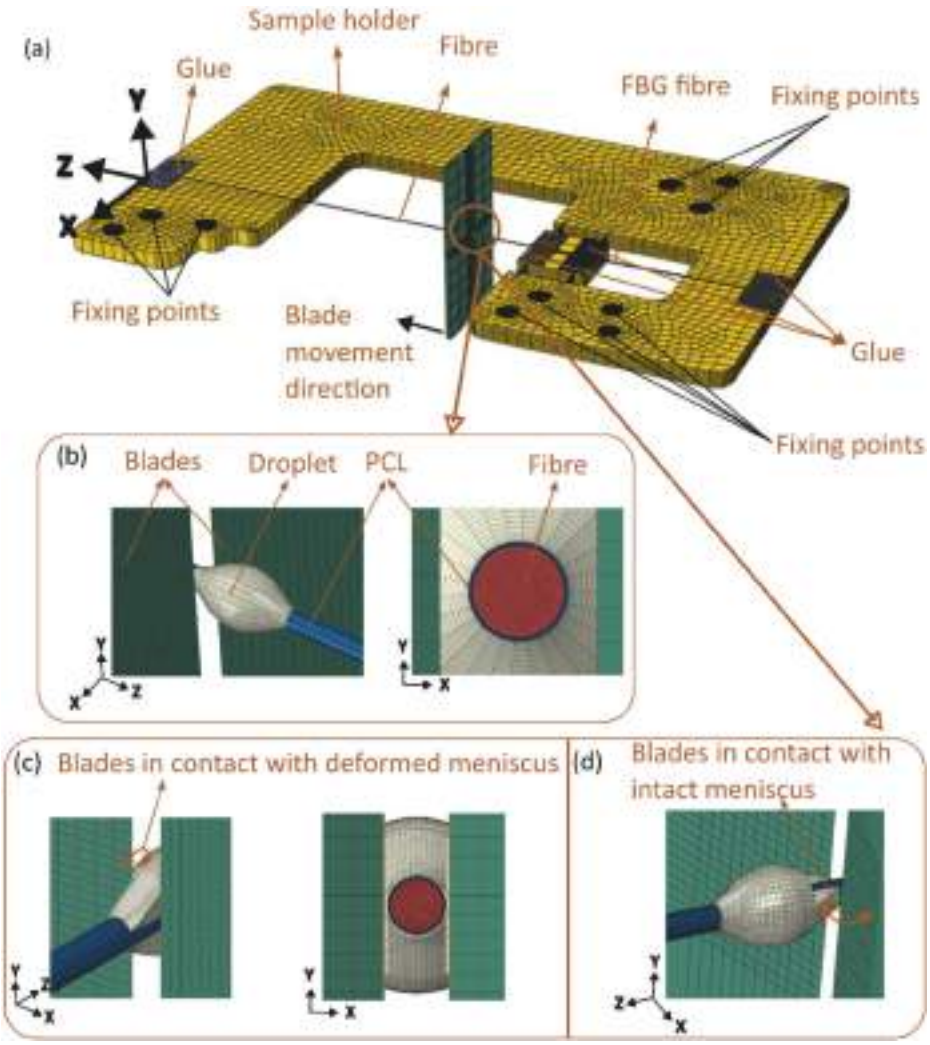

Fig. 4. Representation of (a) 3D assembly of the simulation setup, (b) H0 case showing different components of the FE model, (c) H1 case showing the deformed droplet and their corresponding blade contacts with deformed meniscus, (d) H1 case showing the deformed droplet and their corresponding blade contacts with undeformed meniscus.

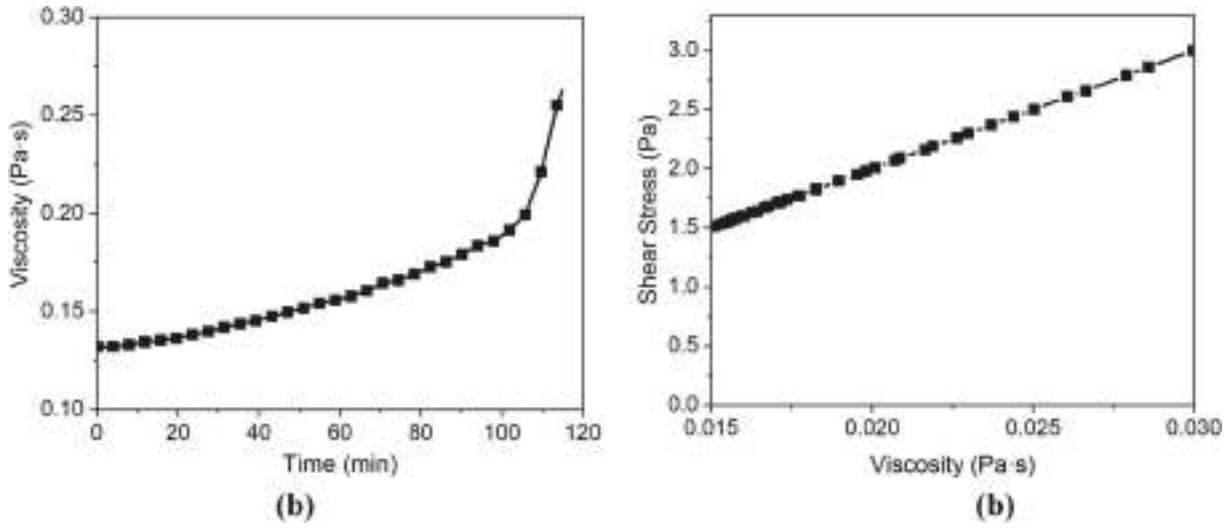

Fig. 5. (a) Evolution of the viscosity of PCL solution overtime at room temperature, (b) Newtonian behaviour of the PCL liquid solution (data were taken after 30 s of soaking time).

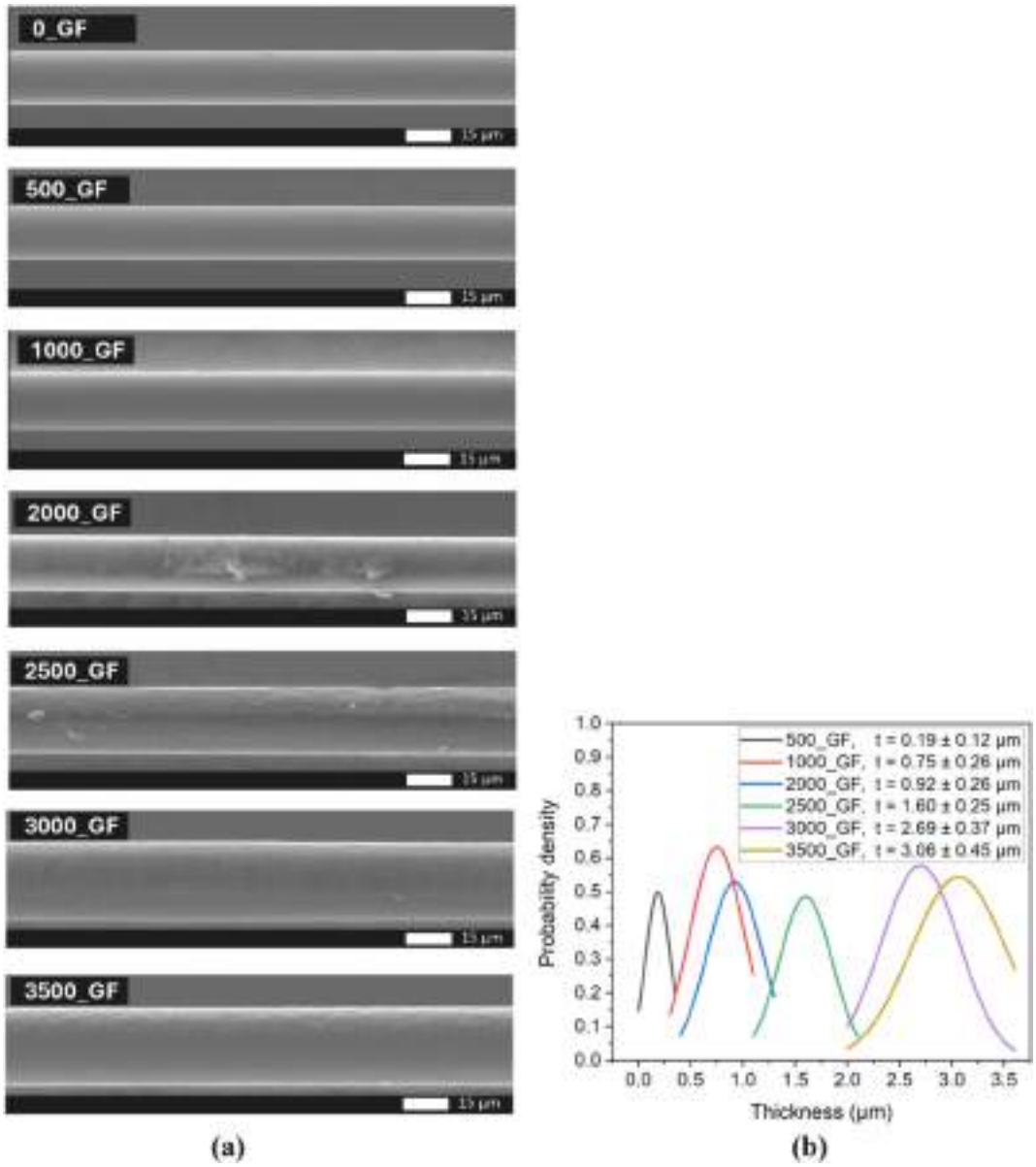

Fig. 6. (a) Morphology of the prepared fibers as a function of the coating speed, (b) normal distribution of PCL coating thickness as a function of the coating speed.

An apparent interfacial shear strength (IFSS) was determined as the slope of the linear regression line relating the maximum shear load (F_{max}) applied to multiple droplets to their embedded area (A), as expressed in Equation (1).

$$F_{max} = IFSS \bullet A + q \quad (1)$$

The embedded area A was calculated as reported in Equation (2), where d is the diameter of the GF and l is length of the droplet.

$$A = \pi dl \quad (2)$$

The intercept (q) in Equation (1) considers the influence of experimental factors such as thermal-oxidative degradation of the matrix resin and residual stresses, as explained by Cai et al. [44,45].

After debonding, the droplets were healed by placing the microcomposites in an oven at 80 °C for 30 min, and then retested as previously described. In this way, interfacial self-healing could be achieved through the physical softening of the PCL coating upon exposure to heat. When heated, the PCL melted and flew, allowing cracks or voids at the fibre-matrix interface to be filled. This restored interfacial adhesion by bringing the polymer chains closer together and physically 'healing' the damage. In addition, minor secondary interactions, such as polymer chain interdiffusion and hydrogen bonding, could further improve adhesion. Four stages of analysis were considered: H0, H1, H2, H3. H0 represented the unhealed stage and it was used to determine the initial fiber-matrix IFSS. H1, H2, H3 represented three consecutive debonding-healing stages and they were used to determine the efficiency of multiple self-healing. The self-healing efficiency (H.E.) was calculated as the ratio between the interfacial shear strength after healing ($IFSS_{H(i)}$) over the initial value ($IFSS_{H0}$), as reported in Equation (3).

$$H.E._{(i)}(\%) = \frac{IFSS_{H(i)}}{IFSS_{H0}} \bullet 100, i = 1, ..3 \quad (3)$$

2.3.6. Finite element (FE) analysis

Full 3D FE simulations were carried out to study microbond tests before and after healing, incorporating the 3D deformation of the droplets. To ensure accurate model generation, a separate set of dedicated microbond test experiments were conducted using a modified sample holder equipped with an integrated Fiber Bragg Grating (FBG) sensor for precise fiber strain measurements. The force and the fiber

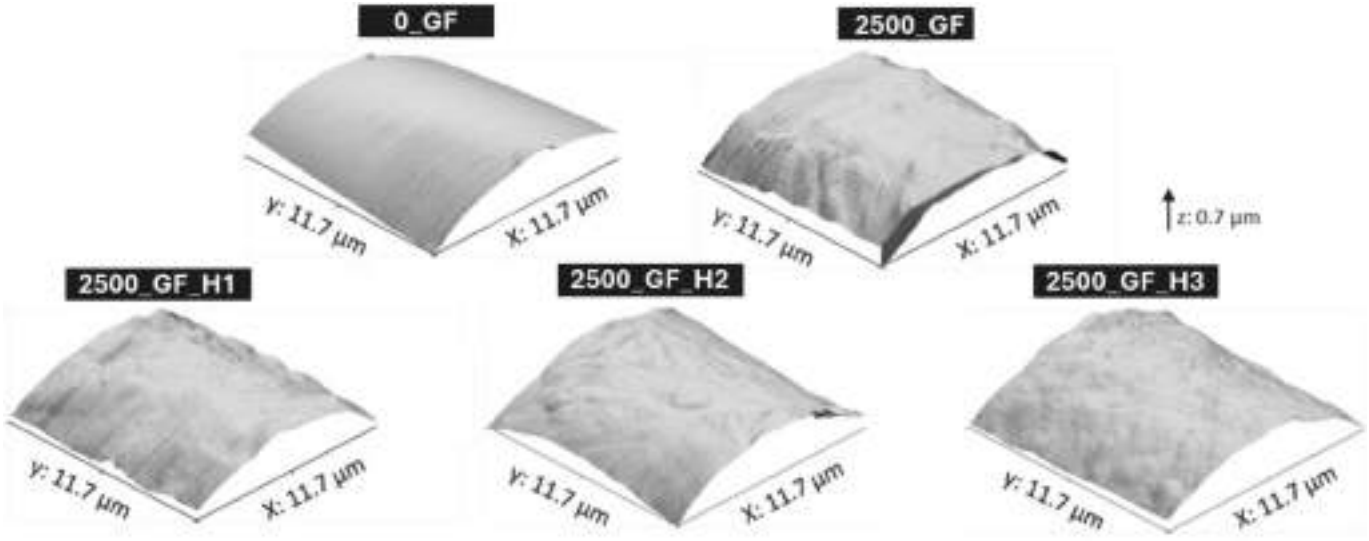

Fig. 7. Example of AFM in height data for samples 0_GF, and 2500_GF, 2500_GF_H1, 2500_GF_H2 and 2500_GF_H3.

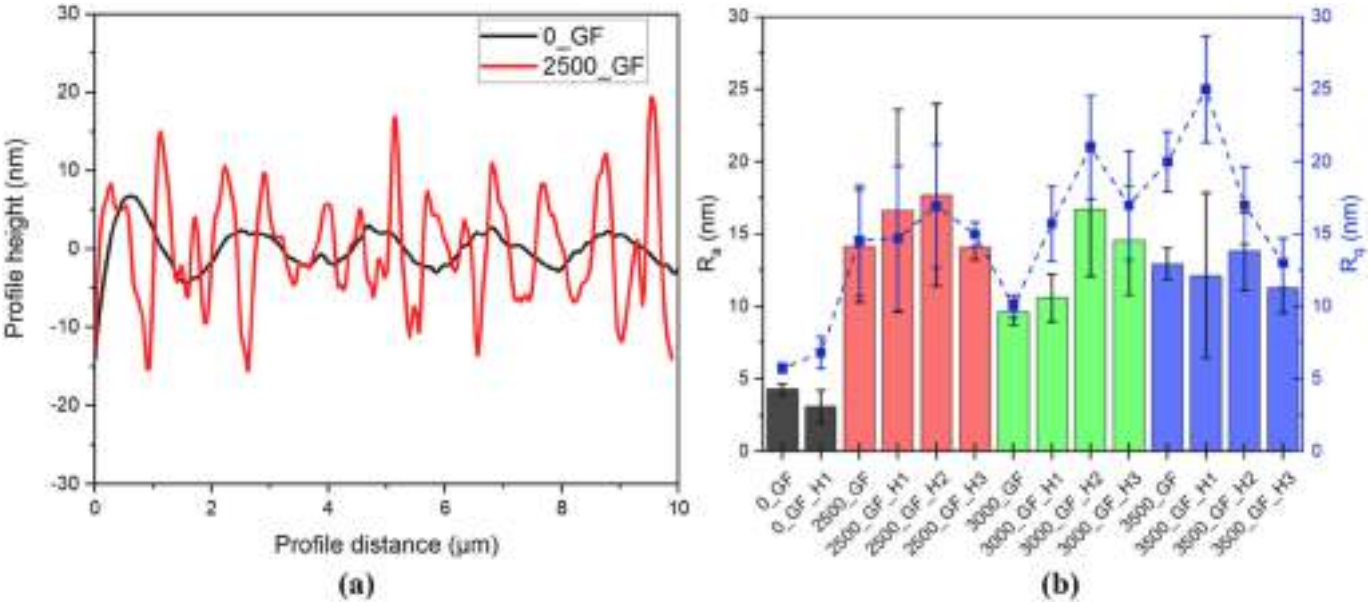

Fig. 8. (a) Example of the profile height of 0_GF and 2500_GF samples measured in the axial direction of the fibers, (b) values of arithmetical mean roughness (R_a) and root-mean-square roughness (R_q) after multiple healing stages.

strain data were crucial for calibrating the interface parameters in the numerical models. A comprehensive description of the sample holder design and implementation for microbond tests is described by Dsouza et al [46]. Two primary studies were carried out in this work. The first analysed the effect of droplet shape changes during subsequent healing steps in microbond tests. The second study examined the effect of coating thickness to support the experimental findings.

The FE model of the microbond test setup with the modified sample holder consisted of an optical FBG fiber (for strain sensing), glass fiber (test filament), epoxy droplet, PCL coating, UV-light cured glue, stainless steel blades and sample holder made of Ti6Al4V. The blades were modelled as rigid bodies, while the epoxy droplet and the PCL coating were modelled as linear elastic with isotropic plasticity. The remaining FE constituents were modelled as linear elastic materials. For the input data of isotropic plasticity, the data points after the yield stress were used from the stress-strain curves obtained from quasi-static tensile tests on 1BA samples following the ISO 527 standard (Fig. S1 (a,b)).

The glass fiber, epoxy droplet and PCL coating were modelled with full integrated elements to capture the deformation more accurately, while the rest of the constituents were modelled with reduced integration to decrease computational costs (see Table 2). The glass fiber and FBG fiber were affixed to the sample holder using tie-constraints. The entire sample holder was modelled to reduce any compliance-related errors and was constrained in all degrees of freedom at the fixing points as shown in Fig. 4a. To simulate blade movement, displacement was provided in +Z direction as shown in Fig. 4a. A frictionless contact model was applied between the blades and the droplet as shown in Fig. 4b.

The droplet and PCL coating were connected using tie contacts. The interface between the PCL coating and the fiber was modelled using Cohesive zone modelling (CZM). The PCL coating was assumed to be a homogeneous layer with a thickness of 1.2 µm and was assigned the properties of an epoxy-PCL blend containing 10%wt of PCL (EP_10PCL) (Fig. S1a). This can be attributed to the curing and thermal healing

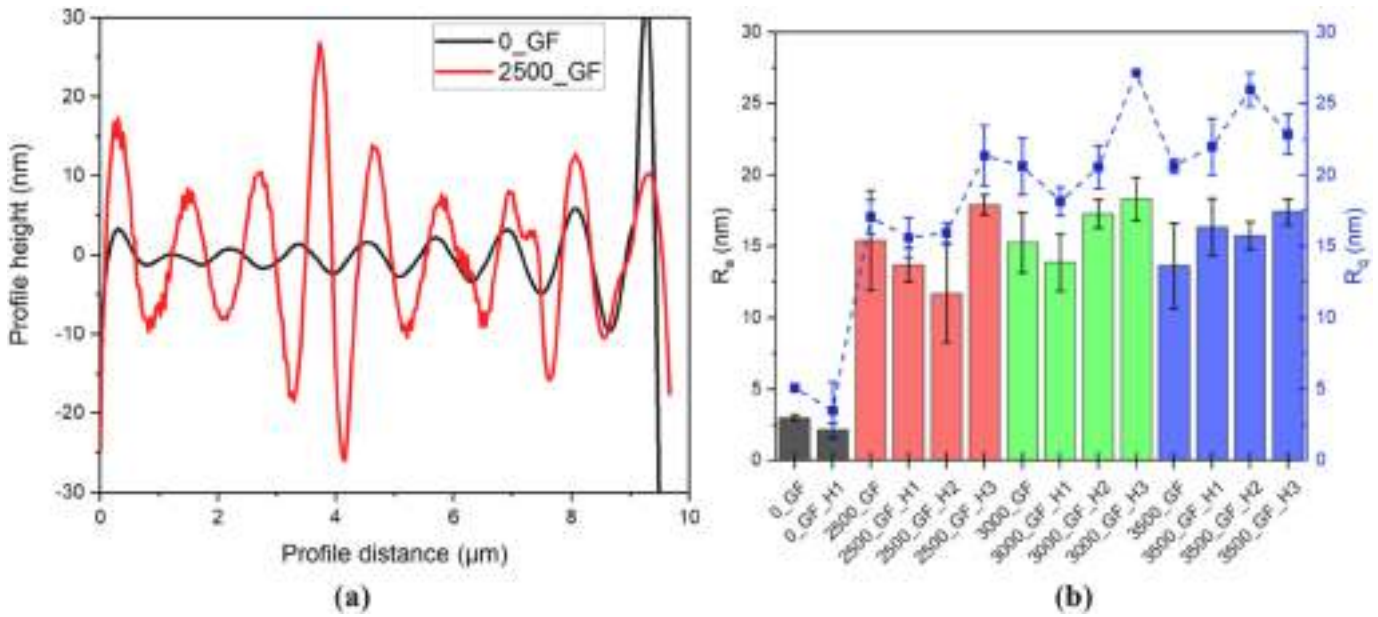

Fig. 9. (a) Example of the profile height of 0_GF and 2500_GF samples measured in the orthogonal direction of the fibers, (b) values of arithmetical mean roughness (R_a) and root-mean-square roughness (R_q) after multiple healing stages.

treatments, the epoxy chemically reacted with the PCL coating creating a zone with hybrid epoxy-PCL properties as demonstrated by Fourier transform infrared spectroscopy (FTIR) reported in Fig. S2 [46]. For comparison, a simulation using only the PCL properties is included in Fig. S3 of the supplementary data. In addition to the PCL layer thickness of 1.2 μm, parametric FE simulations with varying coating thickness of 0.75 μm, 1.6 μm, 2.6 μm, 3 μm and 5 μm were carried out, and the results were compared with those of the sample without coating.

For the interface, CZM with a mixed-mode bilinear traction-separation law was employed to model the interface between the fiber and the coating. This approach simulated both interfacial damage initiation and propagation. Damage initiation was governed by a quadratic nominal stress criterion (Equation (4)), where τ_s, τ_t and τ_n indicated the nominal stresses when the deformation is either purely normal to the interface or purely in the first or the second shear (twist) direction. The damage propagation was assigned to a power law (Equation (5)), where G_I, G_{II} and G_{III} indicated the work done by the tractions and their conjugate relative displacements in the normal, first, and second shear (twist) directions. The corresponding values for critical stresses ($\tau_{s_{cr}}$, $\tau_{t_{cr}}$ and $\tau_{n_{cr}}$) and fracture energies ($G_{I_{cr}}$, $G_{II_{cr}}$ and $G_{III_{cr}}$) were assumed to be identical in all three directions. These values were calibrated iteratively using experimental force and fiber strain data from the FBG sensor, with the H0 stage serving as the baseline for achieving accurate values (Fig. 4b). A detailed description of the calibration process is reported by Dsouza et al. [47].

$$\max\left\{\frac{\tau_s}{\tau_{s_{cr}}}\right\}^2+\left\{\frac{\tau_t}{\tau_{t_{cr}}}\right\}^2+\left\{\frac{\tau_n}{\tau_{n_{cr}}}\right\}^2=1 \tag{4}$$

$$\left(\frac{G_I}{G_{I_{cr}}}\right)^{\alpha}+\left(\frac{G_{II}}{G_{II_{cr}}}\right)^{\alpha}+\left(\frac{G_{III}}{G_{III_{cr}}}\right)^{\alpha}=1 \quad \textit{wherein} \quad \alpha=1 \tag{5}$$

Every simulation set was carried out in two steps. In the first step, a thermal cool-down loading step ($\Delta T = 50\ ^\circ C$) was applied prior to blade loading to simulate the residual stresses induced during the droplet curing process due to the mismatch in coefficients of thermal expansion between the droplet, PCL, and the fiber. Four sets of simulations were carried out to study the droplet healing process (H0, H1, H2 and H3) and the corresponding effect of droplet shape is studied. In addition, seven sets of simulations were conducted to study the effect of coating thickness.

To simulate the H1 stage, the previously calibrated values of interface parameters were used. This simulation incorporated the specific 3D deformed droplet geometry obtained from the H0 case (Fig. 4c). This deformed geometry was refined to create a suitable CAD model for meshing and subsequent use in H1 simulations. Note that due to the parallel blade geometry in the H0 case, the droplet deformation was non-uniform (Fig. 4d). The H1 stage was tested with both deformed and undeformed meniscus scenarios, maintaining constant interface parameters. All simulations were performed using Dassault Systèmes' Abaqus.

3. Results and discussion

3.1. Rheological characterization of PCL liquid solution

The viscosity of the PCL liquid solution was analysed to control the coating thickness [41]. From Fig. 5a, a fairly steady increase in viscosity can be seen over time due to the evaporation of solvents. At about 1 h 45 min the behaviour of the solution changes significantly. It stops behaving like a liquid and enters a gel-like state. However, since the deposition process takes approximately 10 min, it is reasonable to consider the solution viscosity as constant. Additionally, the PCL liquid solution results to behave like a Newtonian fluid, as shown in Fig. 5b, which behaviour is request in the fluid coating theory.

3.2. Morphological characterization of the coated fibers

In Fig. 6a, the surface morphology of the prepared samples is observed as a function of the coating speed. 0_GF has a clean and smooth fiber surface. By increasing the coating speed, the PCL coating is deposited on GFs as a uniform layer without substantial discontinuities or irregularities. The uniformity of the coatings is important to ensure consistent interfacial properties along the fiber-matrix embedded length. Just some minor dust particles are visible on sample 2500_GF, which can be attributed to environmental contaminations within the laboratory.

Additionally, ImageJ (version 1.53a) software was utilized to measure both the fiber diameter and the coating thickness. Presuming normally distributed thickness variation, the PCL coating thickness (t) is shown in Fig. 6b and plotted as the function of the coating speed. It can

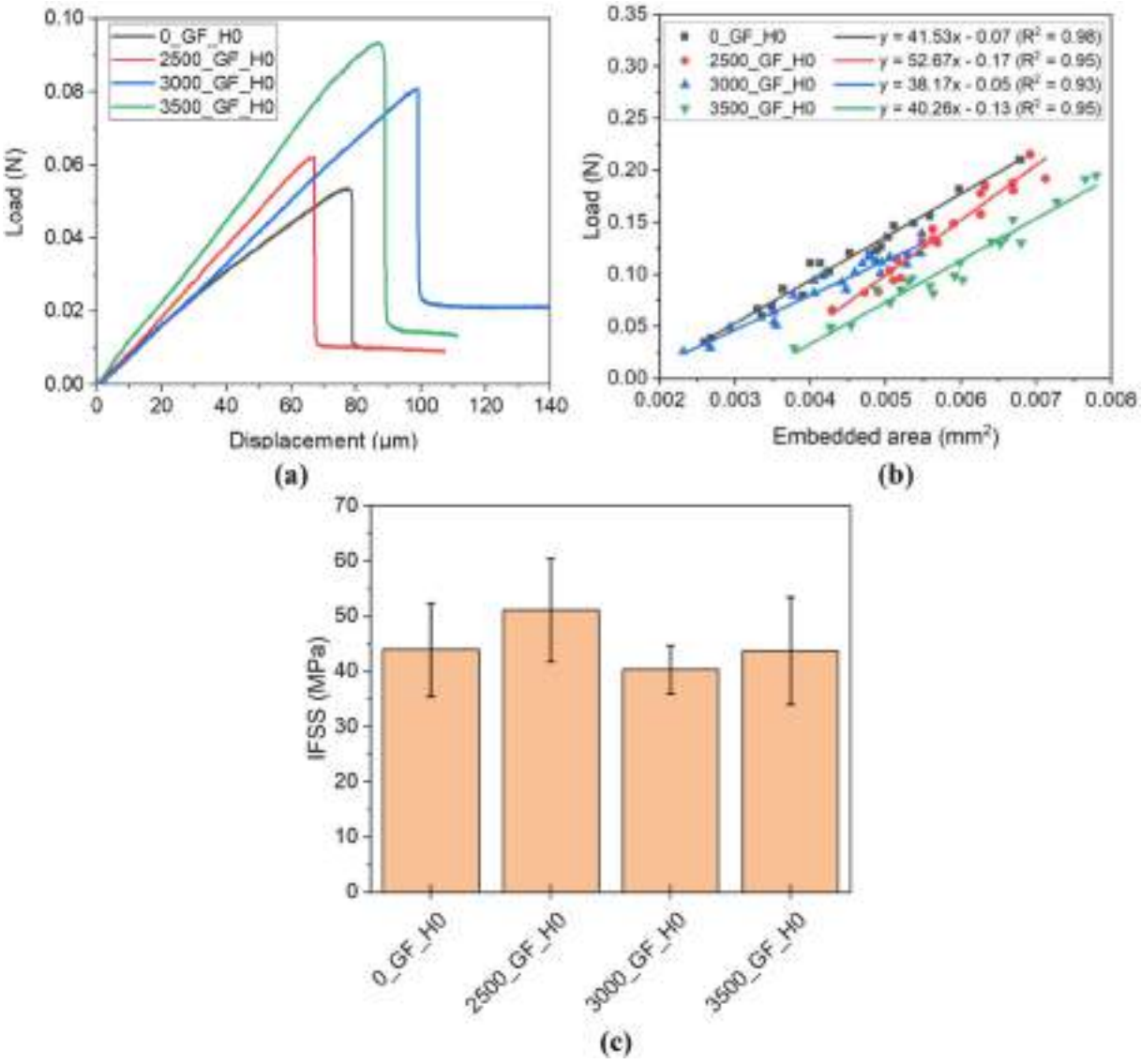

Fig. 10. (a) Representative load-displacement curves from microdebonding tests on unhealed GF/EP samples, (b) examples of the linear regression line of the maximum load applied to individual droplets as a function of their embedded area, (b) IFSS values.

be seen that the higher is the coating speed, the thicker is the resulting coating. The mean value of 0_GF diameter is measured equal to 19.6 ± 0.3 μm, while the coating thickness ranges from 0.19 μm of sample 500_GF to 3.06 μm of sample 3500_GF. Coating speeds higher than 3500 μm/s were excluded since they resulted in the formation of PCL micro-droplets, instead of a continuous coating. This is due to the unwanted Plateau-Rayleigh instability, whose phenomenon has been explained by De Ryck et al. [41]. In this study, the samples coated at 2500 μm/s, 3000 μm/s, and 3500 μm/s were selected for further characterization and to assess the self-healing capability, as they exhibited the most abundant and consistent deposition of PCL coating on the fibers.

Fig. 7 shows an example of AFM 3D height data of samples 0_GF and 2500_GF subjected to three multiple self-healing (2500_GF_H1, 2500_GF_H2 and 2500_GF_H3). The 0_GF surface appears clean and smooth, since no sizing and contaminations are present. The application of the PCL coating causes an evident increase of surface roughness, which is also maintained after the multiple self-healing.

In Fig. 8a, a comparison of the profile height of 0_GF and 2500_GF samples measured in the axial direction of the fibers (i.e. to exclude fiber curvature) is shown, while in Fig. 8b the values of the relative arithmetical mean roughness (R_a) and root-mean-square roughness (R_q) of 0_GF and 2500_GF after multiple healing stages are reported. In Fig. 9a, a comparison of the profile height of 0_GF and 2500_GF samples measured in the orthogonal direction of the fibers is shown, while in Fig. 9b the values of R_a and R_q of 0_GF and 2500_GF after multiple healing stages are reported.

From Fig. 8a and 9a, it can be seen that the roughness profile of the coated fibers appears as a topology with increased complexity than 0_GF, shown by sharper peaks and reduced peak width, which increases the area of contact between matrix and fiber. 0_GF shows mean R_a value equal to 4.2 ± 0.3 nm and mean R_q equal to 5.7 ± 0.3 nm in the axial direction. Similar results are obtained in the orthogonal direction, meaning that the roughness of the fiber surface tends to be similar in different directions. The application of the PCL coating enhances the R_a values to 14.1 ± 3.7 nm for 2500_GF, to 9.5 ± 0.8 nm for 3000_GF and to 12.0 ± 1.1 nm for 3500_GF, and R_q values to 14.5 ± 3.8 nm for 2500_GF, to 10.0 ± 0.8 nm for 300 0_GF and to 20.1 ± 1.1 nm for 3500_GF. Again, similar results of R_a and R_q are obtained orthogonally, excluding a preferential dependence of the coating roughness from the direction of the coating process. The consecutive, thermally activated self-healing stages do not significantly affect the R_a and R_q values in both test directions, which means that surface roughness is retained after

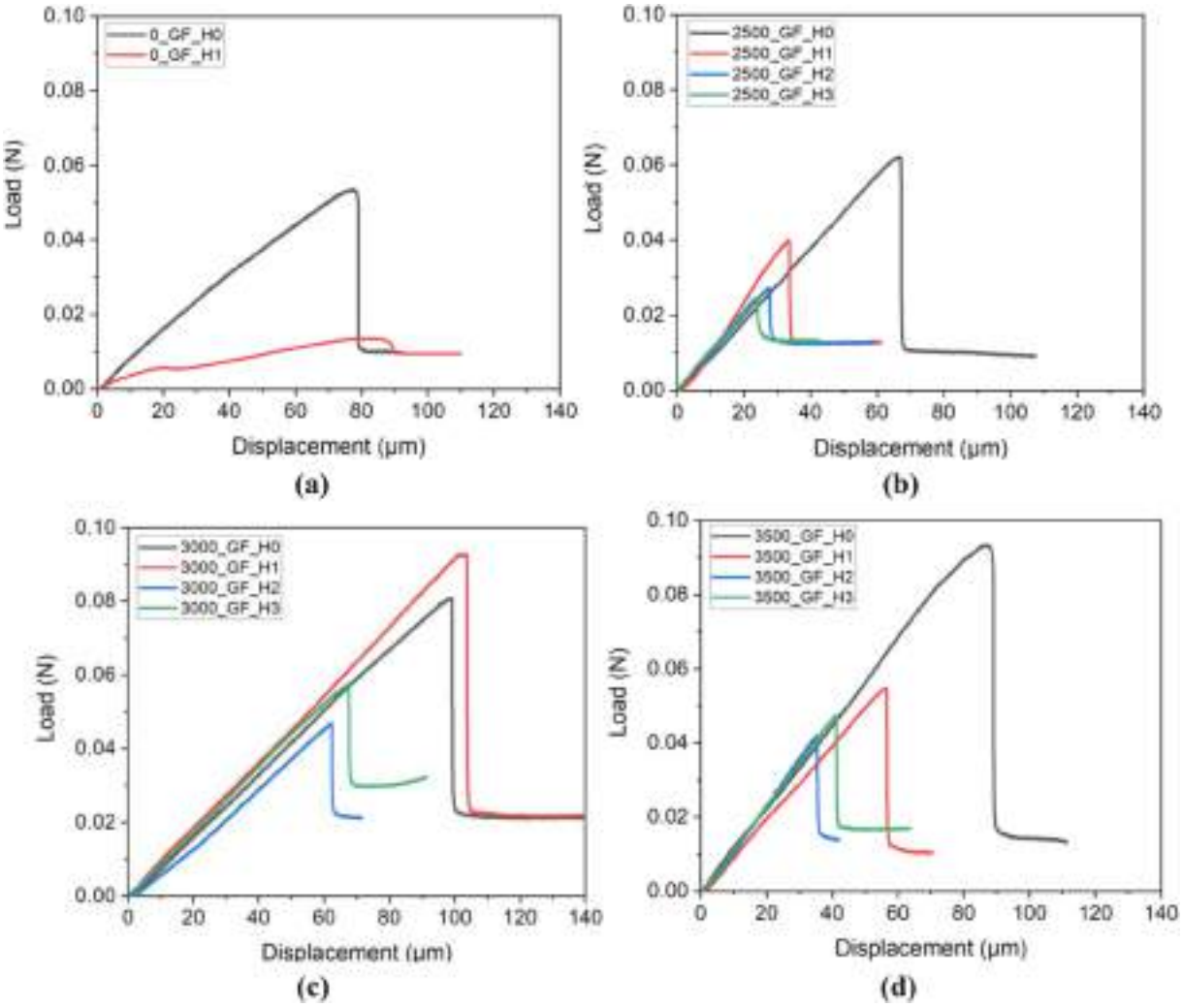

Fig. 11. Examples of load-displacement curves from microdebonding tests on for unhealed and healed interfaces of samples (a) 0_GF, (b) 2500_GF, (c) 3000_GF, (d) 3500_GF, at different healing stages (H0. H1, H2, H3).

consecutive thermal treatments. It is also important to underline that the roughness of the PCL coating could strengthen the mechanical interlocking component of interfacial adhesion.

3.3. Mechanical characterization of the fiber/matrix interphase

3.3.1. Evaluation of the interfacial adhesion properties

IFSS was assessed by microdebonding tests. In Fig. 10a, the load-displacement curves of the prepared unhealed samples are shown. In Fig. 10b, an example of the linear regression relating the maximum load applied to individual droplets as a function of their embedded area is reported. Linear equations and R^2 values are specified. Fig. 10c summarizes the average IFSS values obtained for each sample series.

Fig. 10a shows the typical microdebonding curves that relate the load applied to the droplet and the corresponding displacement: an initial linear region, where the sample is elastic and deforms reversibly, followed by a peak of sudden localized (interface) damage and a plateau corresponding to frictional contributions. From these curves, the maximum values of load where taken and fitted with the corresponding embedded areas, as show in Fig. 10b. The data points show a linear fitting with a regression quality of $R^2 = 0.95$, indicating a strong linear relationship between points with high degree of predictability by the selected IFSS calculation method. High R^2 value implies that the fiber-matrix adhesion remains consistent throughout the entire fiber length. This aspect is particularly important in the case of PCL-coated GF, where high value of R^2 of the fitting suggest a reliable and uniform deposition of the coating on GF. On the other hand, the q values display negative signs (between −0.05 N and −0.17 N), which were also observed by Cai et al. [45]. In Fig. 10c, the IFSS values of the samples are presented. The 0_GF_H0 has an interfacial adhesion with epoxy of 43.9 ± 8.5 MPa. Upon applying PCL coating at different speeds and therefore at different thicknesses, the interfacial adhesion shows no significant changes. In fact, given the overlap of uncertainty, the IFSS values can be considered largely unchanged and the IFSS plateaued. However, a slight improvement in interfacial adhesion is observed for 2500_GF_H0, showing a 16 % increase. This suggests the presence of optimized conditions, such as surface roughness and coating thickness, which may enhance bonding between the glass fibers and epoxy matrix, contributing to the observed improvement.

3.3.2. Evaluation of the interfacial self-healing properties

Microdebonding curves of unhealed and healed interfaces are shown in Fig. 11a-d.

Fig. 11a-d shows that the typical shape of the microdebonding curve is maintained after healing, which demonstrates that the interface has been efficiently healed, also recovering the frictional plateau. This post-debond plateau is needed to overcome the static and dynamic frictions to push the microdrop into motion. This is not true for sample 0_GF_H1, that displays only a slight increase in the load after healing. Hence, the absence of a load higher than the frictional plateau refers to the absence

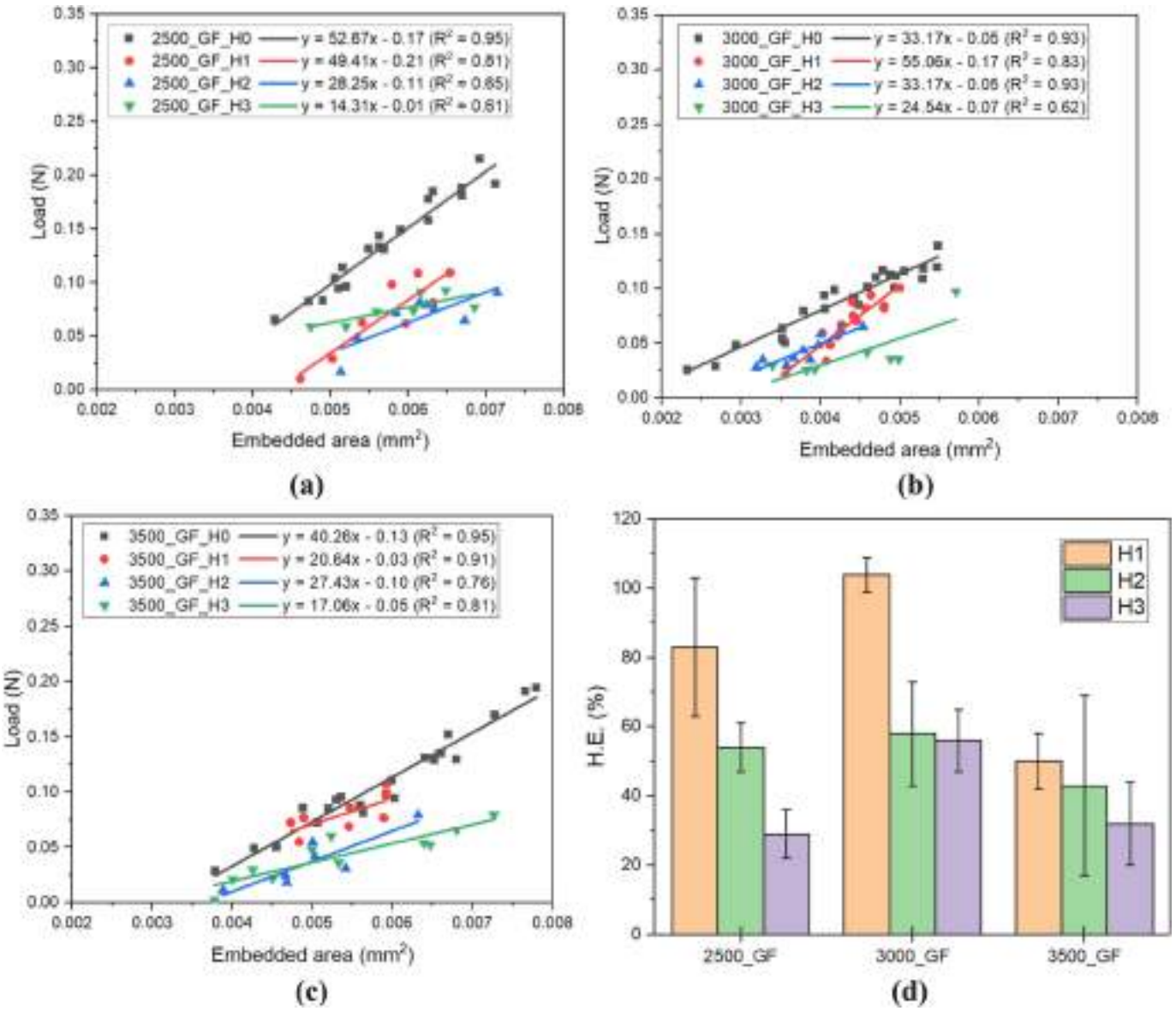

Fig. 12. Linear regression of the maximum force applied to individual droplets and their corresponding embedded areas, (a) 2500_GF, (b) 3000_GF, (c) 3500_GF. Figure (d) shows the healing efficiency values after multiple self-healing stages.

of healing.

In Fig. 12a-c, examples of the linear regressions relating the maximum force applied to individual droplets as a function of their corresponding embedded area are reported, while Fig. 12d summarizes the mean self-healing efficiency (H.E.) values for each sample after multiple self-healing stages. Moreover, in Table S1 of the supplementary materials, the statistical analysis of load data in Fig. 10b and 12a-c is reported, based on a confidence level of 95 %.

In Fig. 12a-c the data points show a linear fit whose R^2 values are not constant. These vary from approximatively 0.95 for H0, to 0.70 for H3. The progressive decrease in R^2 values suggests scatter in adhesion at the fiber-matrix interface after multiple repair stages. This aspect implies also a general decrease of the self-healing efficiency upon multiple self-healing cycles (Fig. 12d). Indeed, after H1 the self-healing efficiency exhibits a value of 100 % in the case of sample 3000_GF_H1, meaning complete re-formation of the adhesive bonds. Lower but still excellent self-healing efficiencies are obtained for 2500_GF_H1 (83 %) and 3500_GF_H1 (50 %). However, as the samples are subjected to repeated healing cycles, the self-healing efficiency exhibits a gradual decline, ultimately approching about 28 % for sample 2500_GF_H3. A possible reason of this decrease is recognized in the progressive modification of the matrix droplet shape observed after repeated microdebonding tests. This hypothesis is supported by Fig. 13, in which the optical images of the evolution of the droplet's shape are reported.

It can be observed that the elliptical shape of the epoxy droplet is well maintained after repeated healing. However, the lack of the meniscus after multiple debonding is evident. During microdebonding tests, the failure of the meniscus is caused by the contact with the blades, as shown in the OPT images of 2500_GF_H2 sample in Fig. 14a,b. In particular, in Fig. 14a the 3D reconstructure of the sample is shown. From this reconstruction, the longitudinal cross section of the sample is extracted (Fig. 14b) where the indentation of EP caused by the blades is visible. The lack of the meniscus caused by the blades may alter the stress state near the fiber/droplet contact point, therefore affecting the resulting values of IFSS [48]. In this sense, a possible cumulative effect may arise, ultimately compromising the adhesion values after multiple stages. Therefore, a FE analysis is presented in the next section to have a deeper comprehension of this phenomenon.

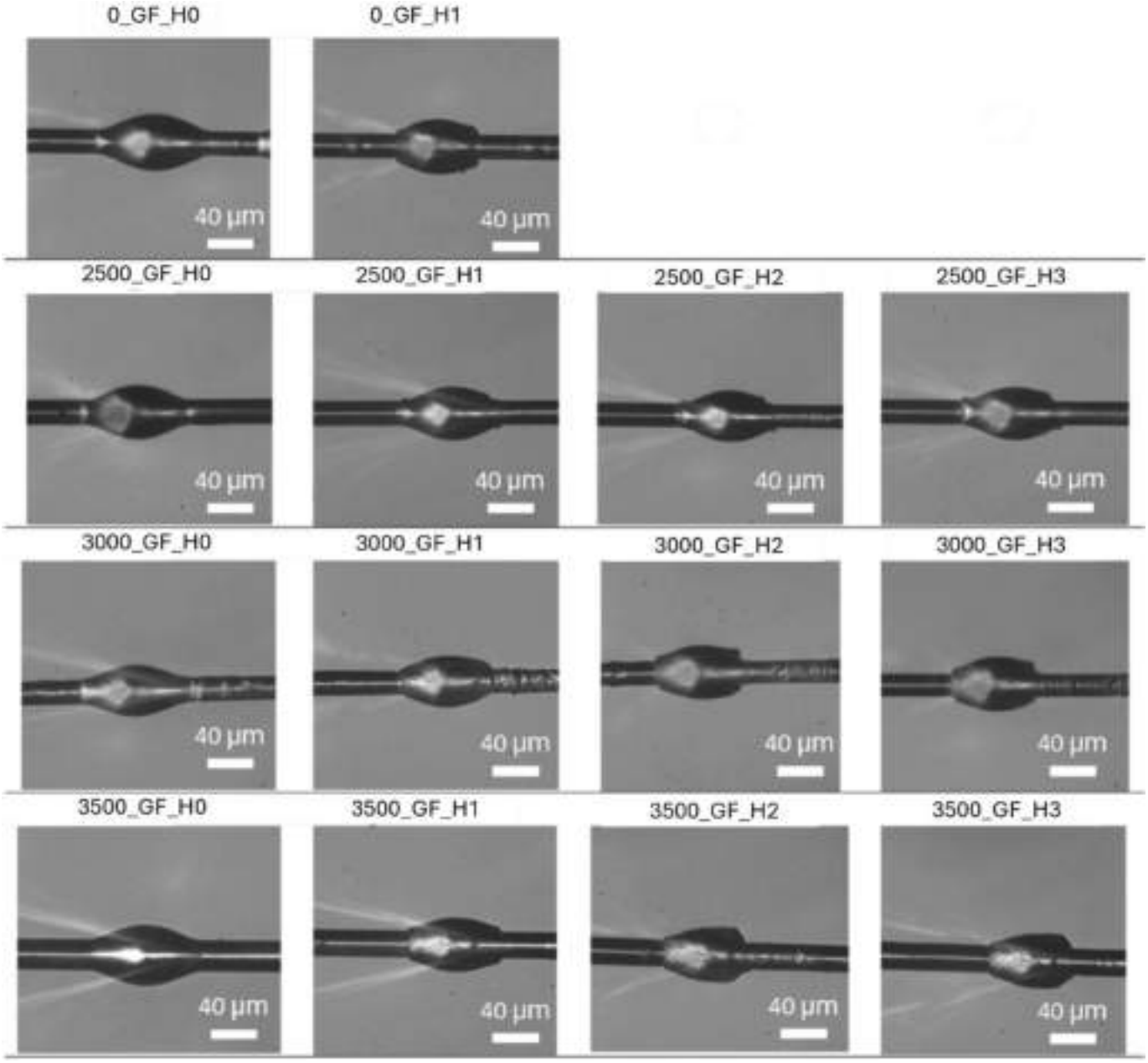

Fig. 13. Optical images of the evolution of the shape of droplet after multiple self-healing stages (H0, H1, H2 and H3).

3.3.3. Finite Element Analysis (FEM) of fiber-droplet contact point

The FE analysis comprised four sequential simulations (H0, H1, H2, and H3), representing different stages in the healing process with different droplet shape. The H0 case was simulated using experimental force and FBG strain data to calibrate the CZM parameters (τ_c and G_c). Through iterative fitting, optimal values of $\tau_c = 43$ N/mm^2 and $G_c = 35$ J/m^2 were obtained. These calibrated values were then held constant for the subsequent H1, H2, and H3 healing simulations. Fig. 15 illustrates the force-displacement curves obtained from these simulations. The corresponding snippets (Fig. 15 i-iii) showcase the deformed droplet geometry and associated von Mises stresses (note: the blades are visualized transparent in the figures to enhance the clarity of droplet deformation).

The H0 simulation curve shows strong agreement with the experimental curve. In particular, even without modelling the frictional slip after droplet's debonding, the simulation captures the non-zero reaction force after debonding. This is attributed to the presence of the film, which the droplet encounters upon debonding and subsequent sliding. The H1, H2, and H3 healing simulations reveal a progressive decrease in peak force due to the shape change (reductions of 25 %, 59 %, and 65 %, respectively, compared to the H0 case). These simulations were conducted with the loading blades in contact with the deformed meniscus, and the areas not in contact with the blades were kept unchanged throughout the subsequent simulations. The observed decrease in the peak force is primarily attributed to the reduction in the embedded area of the fiber-droplet interface in each successive healing step. The evaluation of the dissipated plastic strain energy (ALLPD) at peak force shows that the H0 case exhibits the highest ALLPD, exceeding that of the H1, H2, and H3 cases by approximately 900 % (Supplementary Fig. S4). This large difference is attributed to the significant deformation of the rotationally symmetric meniscus in the H0 case, requiring substantial energy dissipation for deformation and eventual debonding (Fig. S5). These findings collectively suggest that the permanent damage accumulated by a droplet in subsequent microdebonding tests is essential

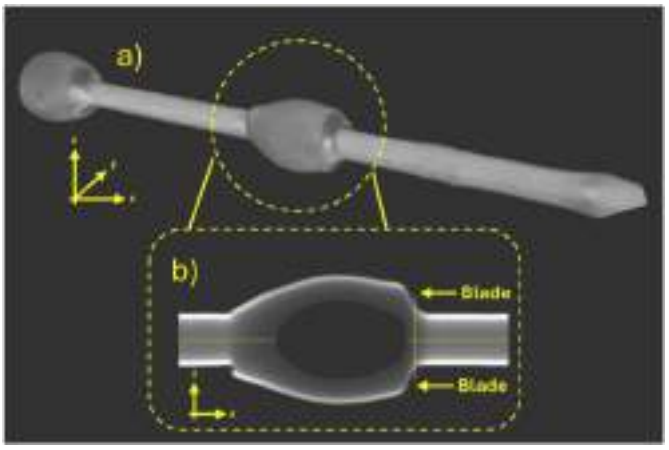

Fig. 14. (a) 3D image and (b) 2D image of 2500_GF_H2 sample from OPT analysis.

behaviour. This simulated effect is of the same magnitude as observed experimentally (Fig. 11a-d). Further studies would be interesting to implicitly model the plastic deformation during phases of simulation with re-iterated and re-bonded CZM interface.

During the MB experiments, the use of parallel blades resulted in droplet deformation confined to the blade-droplet contact region. After debonding, both intact and deformed regions of menisci can be observed, as depicted in Fig. 15(iii). During healing, the film could locally melt due to temperature, consequently causing a random contact between the blades and either the intact or deformed meniscus. To investigate this phenomenon, an additional set of simulations was conducted for the H1 case, specifically focusing on the scenario where the blades load the intact meniscus (Fig. 16a,b). The same interface parameters were maintained.

The results demonstrate that loading the intact region of a deformed (re-done geometry) droplet with the blades leads to a 21 % increase in peak force compared to loading the deformed region of a deformed (re-done geometry) droplet (Fig. 16a). This increase is accompanied by a higher ALLPD, as the intact meniscus region undergoes significant deformation (approximately 900 % higher than its deformed counterpart) (Fig. 16b). By the end of the simulation, the meniscus is entirely deformed, suggesting that subsequent healing stages would likely exhibit a more pronounced drop in peak force compared to scenarios involving an intact meniscus. Clearly, the plastic deformation of droplets is one reason for the higher scatter observed in experiments and fitting of linear curves (and low R^2). In a future development of this work, it will be necessary to understand how to avoid meniscus deformation in order to minimise the underestimation of self-healing efficiency values after multiple stages.

In Fig. 17, the numerical simulation results of the effect of coating

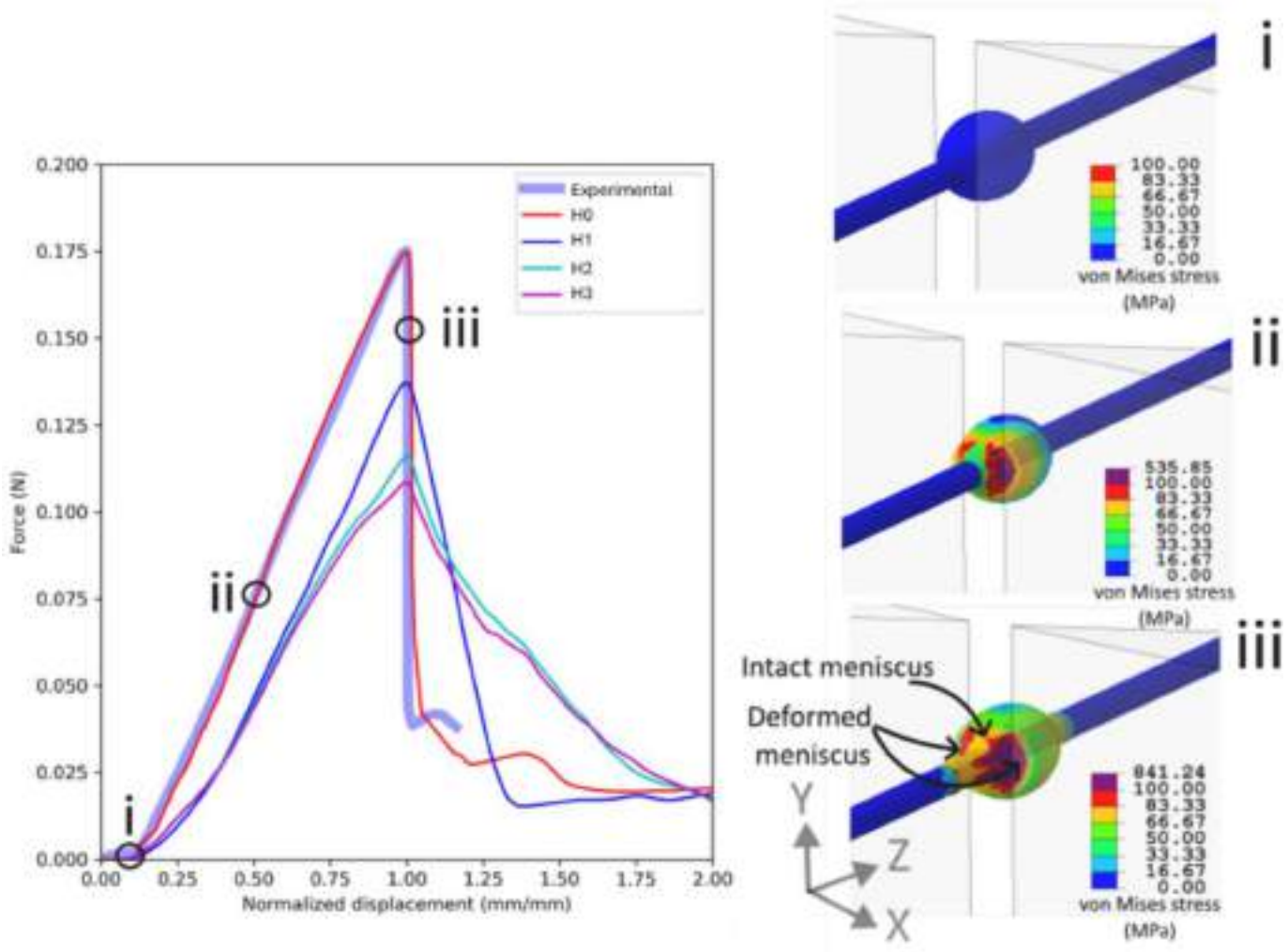

Fig. 15. Force-displacement curves obtained from experiments and simulations (H0, H1, H2, H3). The different test phases (i-iii) and corresponding snippets showcase the deformed droplet geometry and associated von Mises stress.

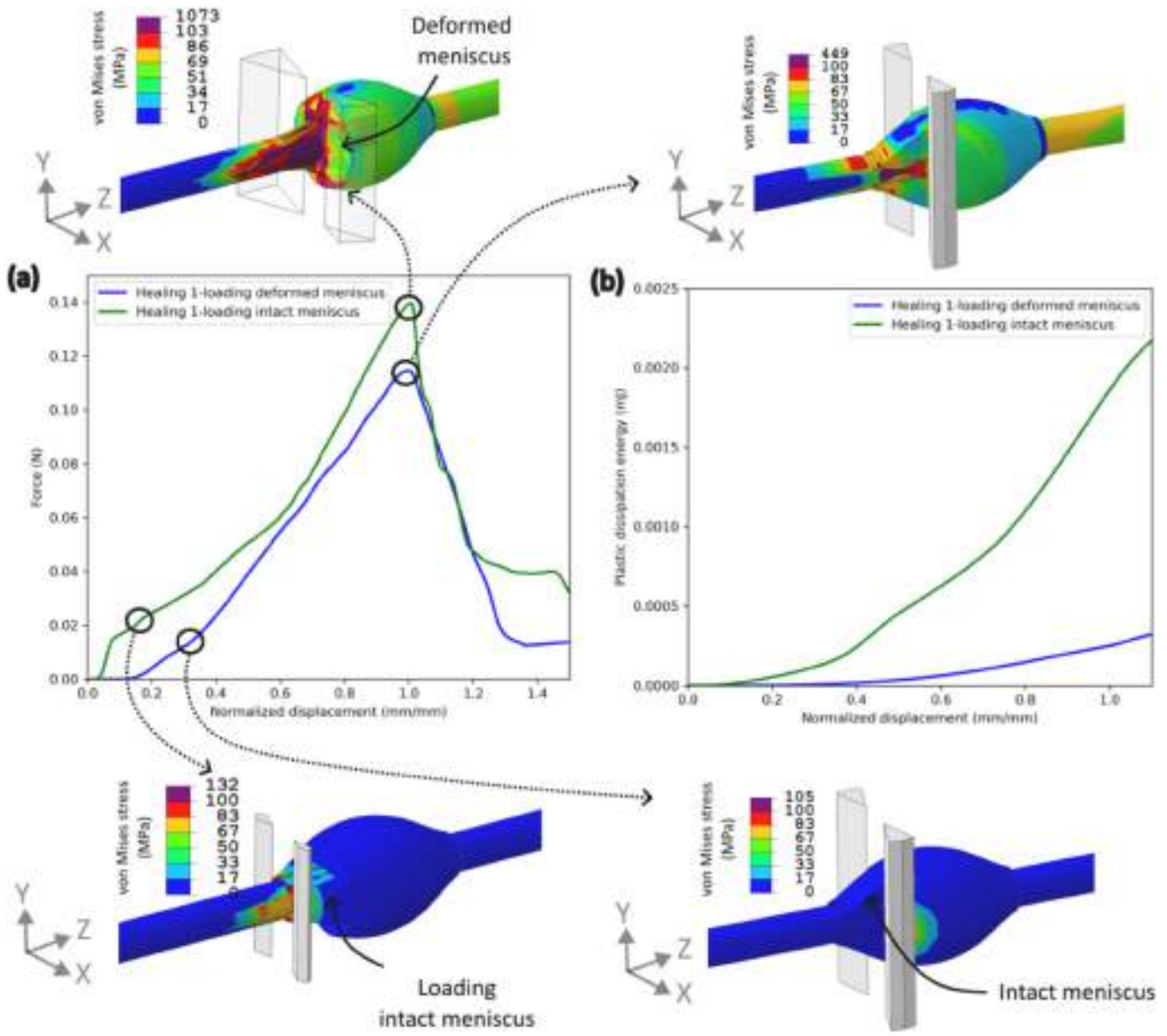

Fig. 16. (a) Force-displacement plots for simulations when loaded on deformed meniscus and intact (re-done geometry) meniscus, (b) corresponding dissipated plastic energy as a function of displacement. Here the displacement is normalized by the corresponding displacement at F_{max}.

thickness on F_{max} are reported, where the percentage increase in F_{max} is calculated relative to the uncoated sample. Coating thickness from 0.75 μm to 5 μm were examined.

The simulations reveal that the F_{max} increases by 10 %–30 % compared to uncoated samples as the coating thickness increased. This increase can be attributed to the mixed epoxy-PCL material properties assigned to the coating layer in simulations, which was also evidenced by FTIR analysis. The curing and thermal healing treatments enhanced the chemical interactions between the epoxy and PCL resulting in a "hybrid zone". As the coating thickness increases the strain energy close to the interface decreases, alsongside the decrease in plastic dissipation energy close to the interface. In addition, as the coating thickness increases, more work is required to debond the epoxy droplet, thereby requiring more energy to initiate the damage at the interface. These results also allign with the findings of Dsouza et al., who reported similar behaviour in their study on additional film thickness affecting the microbond tests [49].

In contrast, experimental results in slight different behaviour. The IFSS improves with increasing coating thickness of up to approximately 1.2 μm, after which IFSS plateaus. This discrepency can be likely attributed to the surface roughness and chemical interactions at the interface. As the coating thickness increases, the chemical bonding and the mechanical interlocking close to the interface may reduce, which reduces the IFSS at greater coating thicknesses. Therefore, this decreases the effectiveness of the hybrid zone (less pronounced hybridization of the epoxy-PCL) near the interface with increased coating thickness. This could be also correlated to the simulation results with only PCL properties assigned to the coating, which drastically reduces F_{max} (see Fig. S3). In summary, up to a critical coating thickness, the hybrid zone acts like an efficient gradient "interphase" enhancing stress transfer and mechanical interlocking which is observed with increase in F_{max} and IFSS.

4. Conclusions

In this work, a continuous poly(ε-caprolactone) (PCL) coating on

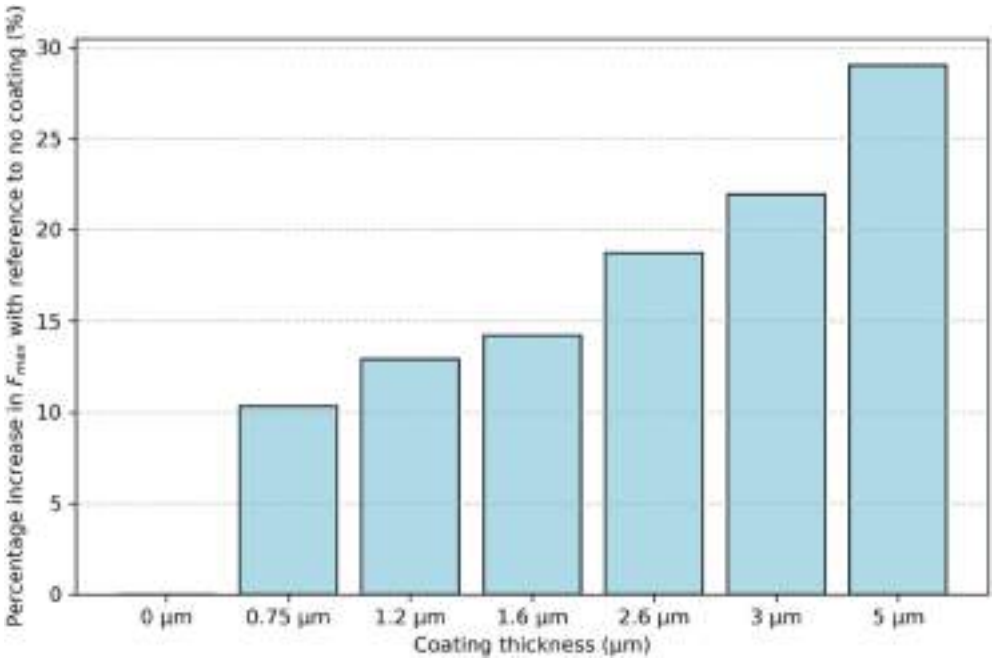

Fig. 17. Numerical simulation results of the effect of coating thickness on F_{max}. The percentage increase in F_{max} is calculated relative to the uncoated sample.

glass fibers (GFs) was developed using fluid coating theory in order to produce glass fibersepoxy microcomposites with self-healing capability. The uniformity and consistency of the coating were confirmed by scanning electron microscopy, which revealed the absence of noticeable discontinuities nor irregularities. The thickness of the PCL coating was found to be dependent on the coating speed, with increased speeds resulting in thicker coatings. Surface roughness was improved given the presence of the PCL layer, as shown by atomic force microscopy (AFM). The PCL-coated fibers were incorporated into microcomposites with epoxy resin (EP), and their performance was evaluated through microdebonding tests. The IFSS improved with increasing coating thickness of up to approximately 1.2 µm, after which IFSS plateaued The interfacial shear strength (IFSS) was improved with increasing coating thickness of up to approximately 1.2 µm, after which plateaued. The interfacial self-healing capability was demonstrated effectively upon thermal activation and re-tested droplets for IFSS. However, repeated healing cycles led to a gradual decrease in self-healing efficiency in terms of IFSS. This was found partly attributed to the cumulative plastic deformation of the EP meniscus. This deformation impacted the stress distribution along the fiber-matrix interface, leading to an underestimation of interfacial adhesion and self-healing efficiency values from the experimental data. Finite element (FE) analysis of the interfacial region was performed to provide deeper insights into the debonding and healing effects. FE analysis involved four simulations (H0, H1, H2, H3), each representing a healing stage with specific deformed geometry. For the initial calibration, experimental data yielded $\tau_c = 43$ N/mm^2 and $G_c = 35$ J/m^2 for the cohesive zone model (CZM) of the interface. Further FE analysis demonstrated that the precise point of blade contact with the droplet deformed in previous test is crucial in understanding the reasoning for decreased peak forces and force-displacement profiles. In a future development of this work, it will be necessary to figure out how to account for the effects of meniscus deformation to minimise the underestimation of self-healing efficiency values after multiple repair stages.

CRediT authorship contribution statement

Laura Simonini: Writing – original draft, Methodology, Investigation, Formal analysis, Data curation, Conceptualization. **Markus Kakkonen:** Software, Investigation. **Royson Dsouza:** Writing – original draft, Software, Investigation, Data curation, Conceptualization. **Mikko Kanerva:** Validation, Supervision, Conceptualization. **Haroon Mahmood:** Validation, Conceptualization. **Andrea Dorigato:** Writing – review & editing, Validation, Supervision. **Alessandro Pegoretti:** Writing – review & editing, Visualization, Validation, Supervision.

Declaration of competing interest

The authors declare that they have no known competing financial interests or personal relationships that could have appeared to influence the work reported in this paper.

Acknowledgements

The authors are greatly thankful to Prof. Devid Maniglio (University of Trento) for the AFM measurements, Prof. Essi Sarlin and Clara Lessa Belone (Tampere Microscopy Center, University of Tampere) for SEM images of neat and coated glass fibers, Lijo George (University of Tampere) for his help in the preparation of the PCL liquid solution, and Pekka Laurikainen (University of Tampere) for the viscosity measurements of the PCL liquid solution.

Appendix A. Supplementary data

Supplementary data to this article can be found online at https://doi.org/10.1016/j.compscitech.2024.110991.

Data availability

Data will be made available on request.

References

[1] J. Karger-Kocsis, H. Mahmood, A. Pegoretti, Recent advances in fiber/matrix interphase engineering for polymer composites, Prog. Mater. Sci. 73 (2015) 1–43.
[2] Y. Yang, R. Boom, B. Irion, D.J. Van Heerden, P. Kuiper, H. De Wit, Recycling of composite materials, Chem. Eng. Process: Process Intensif. 51 (2012) 53–68.
[3] S.J. Park, m.K. Seo, Chapter 8. Composite characterization, in: Interface Science and Technology, Elsevier, 2011, pp. 631–738.
[4] A.G. Koniuszewska, J.W. Kaczmar, Application of polymer based composite materials in transportation, Prog. Rubber Plast. Recycl. Technol. 32 (2016) 1–24.

[5] A. Zaman, S.A. Gutub, M.A. Wafa, A review on FRP composites applications and durability concerns in the construction sector, J. Reinforc. Plast. Compos. 32 (2013) 1966–1988.
[6] A.K. Mohanty, S. Vivekanandhan, J.M. Pin, M. Misra, Composites from renewable and sustainable resources: challenges and innovations, Sci. Sinter. 326 (2018) 536–542.
[7] H. Abouelleil, N. Pradelle, C. Villat, N. Attik, P. Colon, B. Grosgogeat, Comparison of mechanical properties of a new fiber reinforced composite and bulk filling composites, Restor. Dent. &; Endod. 40 (2015) 262–270.
[8] H. Silu, W. Bo, Y. Libo, Interphase and interfacial properties of composite materials, in: Composite Materials: Manufacturing, Properties and Applications, Elsevier, 2021, pp. 151–177.
[9] D.K. Rajak, D.D. Pagar, P.L. Menezes, E. Linul, Fiber-reinforced polymer composites: manufacturing, properties, and applications, Polymers 11 (2019) 1667–1704.
[10] L. Da Silva, A. Ochsner, R. Adams, Handbook of Adhesion Technology, vol. 1, 2011.
[11] L. Simonini, H. Mahmood, A. Dorigato, A. Pegoretti, Evaluation of self-healing capability of a polycaprolactone interphase in epoxy/glass composites, Compos. Appl. Sci. Manuf. 169 (2023) 107539–107548.
[12] H. Mahmood, L. Simonini, A. Dorigato, A. Pegoretti, Graphene deposition on glass fibers by triboelectrification, Appl. Sci. 11 (2021) 3123–3134.
[13] M. Sharma, S. Gao, E. Mader, S. H, L.Y. Wei, J. Bijwe, Carbon fiber surfaces and composite interphases, Carbon fiber surface. Compos. Interphases 102 (2014) 35–50.
[14] L. Xu, L.T. Drzal, Improvement of adhesion between vinyl ester resin and carbon fibers, in: Proceedings of the 13th International Conference on Composite Materials, 2013, pp. 1–10.
[15] M.K. Hossain, M.M.R. Chowdhury, M.B. Salam, J. Malone, M.V. Hosur, S. Jeelani, Improved thermomechanical properties of carbon fiber reinforced epoxy composite using amino functionalized XDCNT, J. Appl. Polym. Sci. 131 (2014) 1–12.
[16] T. Czigan, K. Poloskei, J. Karger-Kocsis, Fracture and failure behavior of basalt fiber mat-reinforced vinylester/epoxy hybrid resins as a function of resin composition and fiber surface treatment, J. Mater. Sci. Technol. 40 (2005) 5609–5618.
[17] L. Simonini, H. Mahmood, A. Dorigato, A. Pegoretti, Tailoring the physical properties of poly (lactic acid) through the addition of thermoplastic polyurethane and functionalized short carbon fibers, Polym. Compos. 44 (2023) 4719–4733.
[18] S. Pozueco, L. Simonini, H. Mahmood, D. Rigotti, M. Kakkonen, A. Riveiro, R. Comesaña, J. Pou, O. Tanhuanpää, O. Kanerva, E. Sarlin, P. Kallio, A. Pegoretti, Influence of CO_2 laser surface treatment of basalt fibres on the mechanical properties of epoxy/basalt composites, Polym. Compos. 45 (2024) 10965–10975.
[19] L. Simonini, R. Canale, H. Mahmood, A. Dorigato, Multifunctional epoxy/carbon composites with a fully reparable interface, Polym. Compos. 45 (2024) 2558–2568.
[20] G. Szebényi, B. Magyar, T. Czigany, Achieving pseudo-ductile behavior of carbon fiber reinforced polymer composites via interfacial engineering, Adv. Eng. Mater. 23 (2021) 2000822–2000829.
[21] A. Cohades, C. Branfoot, S. Rae, I. Bond, V. Michaud, Progress in self-healing fiber-reinforced polymer composites, Adv. Mater. Interfac. 5 (2018).
[22] B.J. Blaiszik, S.L.B. Jkramer, S.C. Olugebefola, J.S. Moore, N.R. Sottos, S.R. Wjite, Self-healing polymers and composites, Annu. Rev. Mater. Res. 40 (2010) 179–211.
[23] A. Dorigato, D. Rigotti, A. Pegoretti, Novel poly(caprolactone)/epoxy blends by additive manufacturing, Materials 13 (2020) 819–837.
[24] H. Mahmood, A. Dorigato, A. Pegoretti, Thermal mending in novel epoxy/cyclic olefin copolymer blends, Express Polym. Lett. 14 (2020) 368–383.
[25] R.C. Zovi, H. Mahmood, A. Dorigato, G. Fredi, A. Pegoretti, Cyclic olefin copolymer interleaves for thermally mendable carbon/epoxy laminates, Molecules 25 (2020) 5347.
[26] M. Kosarli, D.G. Bekas, K. Tsirka, D. Baltzis, D.T. Vaimakis-Tsogkas, S. Orfanidis, G. Papavassiliou, A.S. Paipetis, Microcapsule-based self-healing materials: healing efficiency and toughness reduction vs. capsule size, Compos. B Eng. 171 (2019) 78–86.
[27] I.L. Hia, E.-S. Chan, S.-P. Chai, P. Pasbakhsh, A novel repeated self-healing epoxy composite with alginate multicore microcapsules, J. Mater. Chem. A 6 (2018) 8470–8478.
[28] Y. Wang, Y. Li, Z. Zhang, H. Zhao, Y. Zhang, Repair performance of self-healing microcapsule/epoxy resin insulating composite to physical damage, Appl. Sci. 9 (2019) 4098–4112.
[29] A.R. Jones, B.J. Blaiszik, S.R. White, N.R. Sottos, Full recovery of fiber/matrix interfacial bond strength using a microencapsulated solvent-based healing system, Compos. Sci. Technol. 79 (2013) 1–7.
[30] Z. Hu, D. Zhang, F. Lu, W. Yuan, X. Xu, Q. Zhang, H. Liu, Q. Shao, Z. Guo, Y. Huang, Multistimuli-responsive intrinsic self-healing epoxy resin constructed by host–guest interactions, Macromolecules 51 (2018) 5294–5303.
[31] N.K. Guimard, K.K. Oehlenschlaeger, J. Zhou, S. Hilf, F.G. Schmidt, C. Barner-Kowollik, Current trends in the field of self-healing materials, Macromol. Chem. Phys. 213 (2012) 131–143.
[32] H. Mahmood, A. Dorigato, A. Pegoretti, Healable carbon fiber-reinforced epoxy/cyclic olefin copolymer composites, Materials 13 (2020) 2165–2180.
[33] D. Perin, A. Dorigato, A. Pegoretti, Thermoplastic self-healing polymer blends for structural composites: development of polyamide 6 and cyclic olefinic copolymer blends, J. Appl. Polym. Sci. 140 (2023) 53751–53769.
[34] W. Zhang, J. Duchet, G. Jf, Self-healable interfaces based on thermo-reversible Diels–Alder reactions in carbon fiber reinforced composites, J. Colloid Interface Sci. 430 (2014) 61–68.
[35] E. Malikmammadov, T.E. Tanir, A. Kiziltay, V. Hasirci, N. Hasirci, PCL and PCL-based materials in biomedical applications, J. Biomater. Sci. 29 (2018) 863–893. *Polymer edition*.
[36] L. Cabedo, J. Luis Feijoo, M. Pilar Villanueva, J.M. Lagarón, E. Giménez, Optimization of biodegradable nanocomposites based on a PLA/PCL blends for food packaging applications, in: Proceedings of the Macromolecular Symposia, 2006, pp. 191–197.
[37] R.M. Mohamed, K. Yusoh, A review on the recent research of polycaprolactone (PCL), in: Proceedings of the Advanced Materials Research, 2016, pp. 249–255.
[38] T.K. Dash, V.B. Konkimalla, Polymeric modification and its implication in drug delivery: poly-ε-caprolactone (PCL) as a model polymer, Mol. Pharm. 9 (2012) 2365–2379.
[39] D.S. Boucher, Solubility parameters and solvent affinities for polycaprolactone: a comparison of methods, J. Appl. Polym. Sci. 137 (2020).
[40] R. Cescato, D. Rigotti, H. Mahmood, A. Dorigato, Thermal mending of electroactive carbon/epoxy laminates using a porous poly (ε-caprolactone) electrospun mesh, Polymers 13 (2021) 2723–2744.
[41] A. De Ryck, D. Quéré, Inertial coating of a fibre, J. Fluid Mech. 311 (1996) 219–237.
[42] D. Quere, Fluid coating on a fiber, Annu. Rev. Fluid Mech. 31 (1999) 347–384.
[43] P. Laurikainen, M. Kakkonen, M. Von Essen, O. Tanhuanpää, P. Kallio, E. Sarlin, Identification and compensation of error sources in the microbond test utilising a reliable high-throughput device, Compos. Appl. Sci. Manuf. 137 (2020) 105988–105996.
[44] G. Cai, M. Wada, I. Ohsawa, S. Kitaoka, T. J, Influence of treatment with superheated steam on tensile properties of carbon fiber, Compos. Appl. Sci. Manuf. 107 (2018) 555–560.
[45] G. Cai, M. Wada, I. Ohsawa, S. Kitaoka, J. Takahashi, Interfacial adhesion of recycled carbon fibers to polypropylene resin: effect of superheated steam on the surface chemical state of carbon fiber, Compos. Appl. Sci. Manuf. 120 (2019) 33–40.
[46] J. Barros, I. Dos Santos Silva, N.G. Jaques, M.V. Fook, R.M. Wellen, Influence of PCL on the epoxy workability, insights from thermal and spectroscopic analyses, Polym. Test. 89 (2020) 106679–106690.
[47] R. Dsouza, P. Antunes, M. Kakkonen, J. Jokinen, E. Sarlin, P. Kallio, M. Kanerva, 3D interfacial debonding during microbond testing: advantages of local strain recording, Compos. Sci. Technol. 195 (2020) 108163–108172.
[48] J.T. Ash, W.M. Cross, D. Svalstad, J.J. Kellar, L. Kjerengtroen, Finite element evaluation of the microbond test: meniscus effect, interphase region, and vise angle, Compos. Sci. Technol. 63 (2003) 641–651.
[49] R. Dsouza, M. Kakkonen, A. Prapavesis, E. Sarlin, P. Antunes, A. Van Vuure, P. Kallio, M. Kanerva, Does a polymer film due to Rayleigh-instability affect interfacial properties measured by microbond test? Compos. Interfac. 15 (2024) 1–27.